A comparison of displaced phase centre antenna and along-track interferometry techniques for RADARSAT-2 ground moving target indication

Shen Chiu and Chuck Livingstone

Abstract. Canada's RADARSAT-2 commercial synthetic aperture radar (SAR) satellite will have an experimental mode that will permit ground moving target indication (GMTI) measurements to be made. In this mode of operation, the radar antenna is partitioned into two subapertures that sequentially observe the scene of interest from the same point in space. Two of the GMTI processing approaches currently being explored are examined in this paper. One utilizes the displaced phase centre antenna (DPCA) clutter-cancellation technique to provide subclutter visibility for dim, slowly moving objects. The other is based on the along-track interferometry (ATI) technique, in which magnitude and phase information of the targets' interferograms are exploited to extract them from the background clutter. In this paper the performance of each processor is examined for three RADARSAT-2 slant-range resolutions: 12.5, 3.0, and 1.5 m. The study focuses on the influence of SAR resolution cell size on the GMTI processor performance. Results indicate that, as SAR slant-range resolution increases, the SAR ATI improves in performance, whereas the SAR DPCA does not.

Résumé. Le satellite radar à synthèse d'ouverture (RSO) commercial canadien RADARSAT-2 disposera d'un mode expérimental qui lui permettra de réaliser des mesures GMTI (« ground moving target indication » – indication de cible mobile au sol). Dans ce mode d'opération, l'antenne radar est partitionnée en deux sous ouvertures qui observent de façon séquentielle la scène d'intérêt à partir du même point dans l'espace. Deux des approches de traitement GMTI présentement sous analyse sont examinées dans cet article. L'une utilise la technique d'annulation du fouillis d'échos de l'antenne à centre de phase déplacé DPCA (« displaced phase centre antenna ») pour fournir une visibilité sous fouillis des objets peu visibles caractérisés par un mouvement lent. L'autre est basée sur la technique d'interférométrie longitudinale ATI (« along-track interferometry ») dans laquelle l'information sur l'amplitude et la phase des interférogrammes des cibles est exploitée pour permettre de les extraire du fouillis d'échos de fond. Dans cet article, la performance de chacun des processeurs est examinée pour trois résolutions distance–temps de RADARSAT-2 : 12,5, 3,0 et 1,5 m. L'étude s'intéresse à l'influence de la dimension de la cellule de résolution RSO sur la performance du processeur GMTI. Les résultats indiquent que, avec l'accroissement de la résolution distance–temps RSO, la performance du produit RSO ATI s'améliore contrairement au produit RSO DPCA qui ne change pas.
[Traduit par la Rédaction]

Introduction

Until recently, the detection and tracking of moving targets have been primarily of military concern and have been operationally supported by specialized airborne sensors. With the rapid evolution of radar technology it is now feasible to economically create spaceborne sensors to perform moving target detection and measurement functions. From a military viewpoint, these spaceborne systems have the potential to significantly augment existing operational capabilities. From a civilian viewpoint, spaceborne moving target measurements can provide a previously unavailable land and sea traffic monitoring capability that may prove to be very valuable in designing, monitoring, and controlling transportation infrastructures. Canada's RADARSAT-2 commercial synthetic aperture radar (SAR) satellite will have an experimental mode that will allow ground moving target indication (GMTI) measurements to be made. This mode of operation is also called MODEX (moving object detection experiment). The RADARSAT-2 MODEX is the world's first attempt to implement a limited-function GMTI onboard a commercial

SAR satellite. Although the subset of possible GMTI operating modes available from a radar of this type is small, such a radar could be used to validate GMTI parameters and algorithms needed for more sophisticated radars. Preliminary information on the RADARSAT-2 MODEX configuration can be found in Luscombe (1995) and Livingstone (1998). **Table 1** lists some of the current MODEX sensor characteristics and design parameters. In the MODEX mode, the spacecraft's radar antenna is partitioned into two subapertures that sequentially observe in time the scene of interest from the same point in space to detect temporal changes. The signal is transmitted at full antenna aperture, and data are simultaneously and coherently received from both subapertures and then downlinked in parallel channels for processing that extracts

S. Chiu[1] and C. Livingstone. Space-Based Radar Group, Radar Systems Section, Defence R&D Canada – Ottawa, 3701 Carling Avenue, Ottawa, ON K1A 0Z4, Canada.

[1]Corresponding author (e-mail: shen.chiu@drdc-rddc.gc.ca).

moving target radial speeds in their SAR image context. The radar architecture does not allow azimuth beam steering needed for sector-scan and dwell functions found in operational airborne GMTI radars (Erwin, 2001). The ground processing infrastructure for the MODEX is presently being developed based on a theoretical understanding of the measurement process, augmented and validated by airborne SAR GMTI experiments (Livingstone et al., 2002) and by simulation studies (Chiu, 2000a; 2000b) that emulate the RADARSAT-2 radar performance and observation geometries. The latter is carried out using a space-based radar GMTI simulator, called SBRMTISIM, to test the extrapolation of airborne results to the RADARSAT-2 operating parameters and observation geometries.

Two of the SAR GMTI processing approaches currently being developed at Defence R&D Canada – Ottawa (Sikaneta et al., 2003) are examined and compared in this paper. One utilizes the SAR displaced phase centre antenna (DPCA) clutter-cancellation technique (Dickey and Santa, 1953; Raney, 1971) to provide subclutter visibility for dim, slowly moving targets. The other is based on the SAR along-track interferometry technique (Shapiro et al., 1972; Zisk, 1972; Goldstein and Zebker, 1987), where magnitude and phase information of the slowly moving targets is exploited to extract targets from the dominant clutter background. Owing to the nature of SAR processing, the moving target signal is azimuthally shifted and added vectorially to the clutter signal at the shifted position in the SAR image. When the interferogram is formed from the "fore-and-aft" apertures, the SAR along-track interferometry (ATI) complex signals of the moving target become contaminated with clutter that lies near the zero-phase line in the complex plane (Gierull, 2002b; Chiu, 2003). The effect of clutter contamination may be reduced if the physical size of the target is comparable to the area of the resolution cell or if the resolution cell size is decreased by increasing the signal bandwidth, in which case the performance of the SAR ATI processor is expected to improve. The goal of the present investigation is to examine the influence of the SAR resolution cell size (particularly, the slant-range resolution) on the performance of the two processors using computer modeling and simulation. The performance of the two approaches is examined for three slant-range resolutions, namely 12.5 m (12 MHz), 3 m (50 MHz), and 1.5 m (100 MHz). At the incidence angle (30°) used in this analysis, the corresponding ground range resolutions are 25, 6, and 3 m.
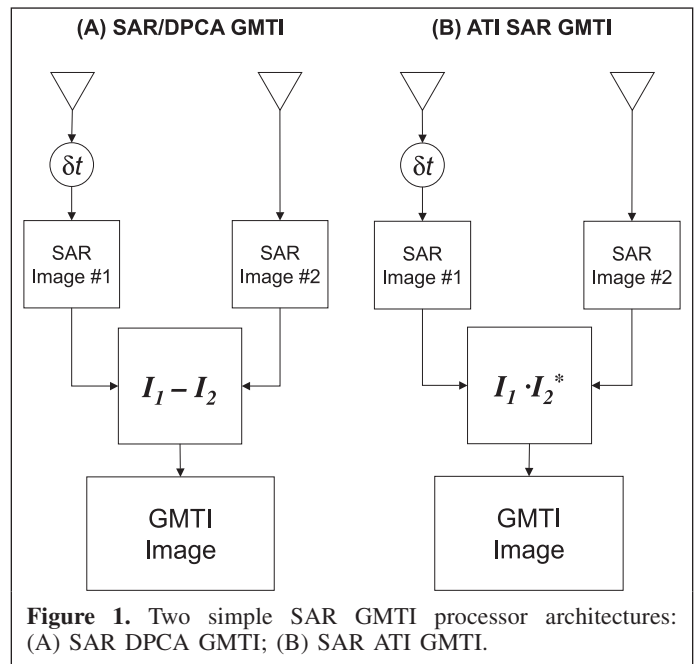
GMTI processing methods

SAR DPCA

Two of the proposed GMTI processor architectures for RADARSAT-2 MODEX are shown in **Figure 1**. The SAR DPCA processor (**Figure 1A**) is the limiting case of a two-beam DPCA clutter canceller. The pulses from the leading antenna are delayed by DPCA time δt to effectuate the DPCA condition, that is, to coregister the fore (image 1) and aft (image 2) images (see **Figure 1**). SAR processing is then performed on

Table 1. RADARSAT-2 MODEX parameters.

Orbit description	
Type	Circular
Inclination (°)	98.6
Altitude (km)	800
Active array	
Length (m) × width (m)	15 × 1.5
No. of subapertures	2
Orientation	Long axis forward; elevation boresight ± 29.5° (selectable)
Look geometry	
Nominal incidence angle (°)	10–60
Search type	Strip map
Swath size (km)	25–150
Azimuth beam width (°)	Programmable from 0.21 to 0.63
Detection cell size (m)	Programmable from 25 × 25 to 3 × 3
Waveform	
Band (GHz)	5.405
Bandwidth (MHz)	10–50
Peak radiated power (kW)	2.4 (42 µs pulse); 3.7 (21 µs pulse)
Duty ratio (%)	10
PRF (Hz)	1300–3800
Receiver noise temperature (K)	795.11

Figure 1. Two simple SAR GMTI processor architectures: (A) SAR DPCA GMTI; (B) SAR ATI GMTI.

each channel, and the outputs of the SAR modules are subsequently subtracted to yield a GMTI image. Ideally, the signals from stationary clutter are suppressed to the noise floor of the radar, and only signals from moving targets with sufficient radial velocity remain. When viewed in the complex plane, the suppressed residual clutter appears as a symmetrical noise amplitude distribution about the origin, and moving targets appear as external points as shown in **Figure 2**. Strong,

stationary targets in the radar scene contribute phase noise to the exterior of the central noise distribution and complicate the process of extracting moving targets. When viewed in terms of target velocity, the DPCA clutter cancellation acts as a notch filter with maximum attenuation at zero velocity. Signals from slowly moving targets are attenuated by the filter skirts. The use of the SAR DPCA technique to provide SAR and MTI

Figure 2. Output of the subtractive SAR DPCA processor, showing clutter signals suppressed and moving target signal above the noise floor. The blue diamonds represent clutter and noise signals, and those within red boxes represent target signals.

simultaneously has been discussed by other authors (e.g., Coe and White, 1995; Stockburger and Held, 1995).

SAR ATI

Similarly, the SAR ATI processor uses two displaced phase centres aligned along-track, but instead of taking the difference of the two channels, an interferogram is formed by taking the product of one image with the complex conjugate of the other after the two image datasets have been spatially coregistered (**Figure 1B**). When viewed in the complex plane as a two-dimensional (2D) magnitude (radius) and phase (angle) distribution, the complex signal output of the SAR ATI processor results in a fin-like histogram as seen in **Figure 3**. Here, the stationary scatterers in the imaged terrain are represented by their phase-noise distribution about the positive, real axis. Moving targets appear at nonzero angles (measured from the positive real axis) that are proportional to the radial velocity of the targets. The signal magnitude distribution along the real axis is determined by the statistics of the stationary scene components, and the signal phase distribution (annular function at constant magnitude) is relatively robust with respect to scene homogeneity (Livingstone et al., 2002). The joint magnitude–phase distribution function provides the basis for constant false alarm rate (CFAR) detector design (Chiu, 2002; Gierull, 2002a). The application of the SAR ATI technique to GMTI has also been examined by other investigators (e.g., Soumekh, 1997; Ender, 1999; Moccia and Rufino, 2001).
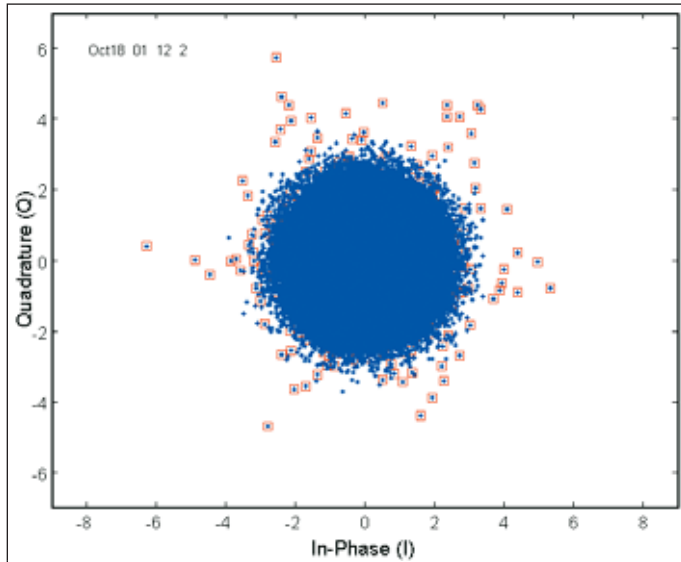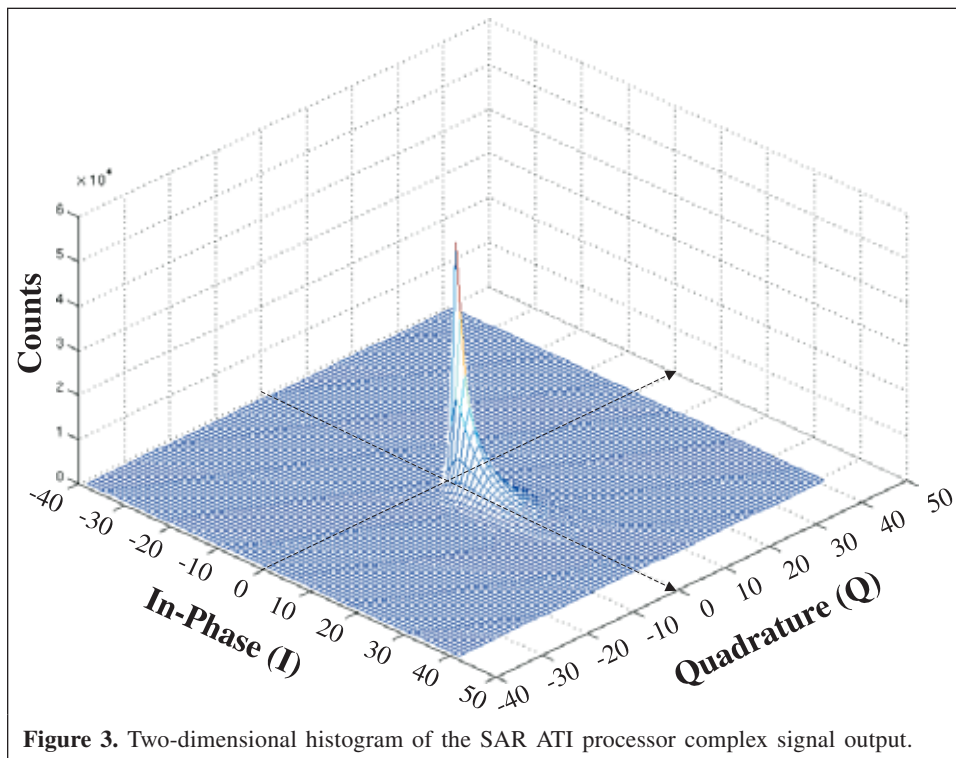

Figure 3. Two-dimensional histogram of the SAR ATI processor complex signal output.

Comparison

The two-aperture SAR DPCA suffers the shortcoming of any two-pulse delay-line canceller in that its output signal is equal to the difference of two slightly different signal vectors and its magnitude, a, is related to the target radial velocity V_r at broadside as

$$a = 2\left|\sin\left(2\pi\frac{V_r\delta t}{\lambda}\right)\right| |S| \tag{1}$$

where δt is the DPCA time, which is equal to the pulse repetition interval (PRI), λ is the wavelength, and S is the signal from either aperture 1 or 2 (assuming $S = S_1 = S_2$). In the modified DPCA (Stimson, 1998), the entire aperture is used for transmission, but only half aperture is used for reception; the spacecraft velocity and the radar pulse repetition frequency (PRF) or PRI^{-1} are adjusted so that during each interpulse period the spacecraft advances a distance precisely equal to half that between the phase centres of the two subapertures. The sine factor in Equation (1) contains the target radial velocity V_r term and, therefore, not only rejects the stationary clutter but also attenuates slowly moving targets. Targets are considered slowly moving if $\sin(2\pi V_r\delta t/\lambda) < 1/2$ or $V_r < \lambda/(8\delta t)$. For a spaceborne system such as RADARSAT-2, moving targets with $V_r < 50$ km/h are, therefore, considered slow.

In contrast, the SAR ATI output is the signal power (as opposed to the signal voltage from the SAR DPCA output) and its magnitude is simply equal to $|S|^2$. Therefore, the slowly moving targets are not attenuated along with the stationary clutter when one utilizes magnitude and phase information for target extraction. At low signal-to-clutter ratios (SCRs), however, the SAR ATI loses its ability to detect slowly moving targets and to correctly estimate their velocities because the system noise (additive thermal noise and multiplicative phase noise of radar) scatters the stationary clutter signal about the real axis in the complex plane. The SCR, which enables a moving target to "rise" above these clustered points, is dependent on the target's velocity. This velocity can be calculated from the interferometric phase

$$\theta_t = \frac{4\pi V_r\delta t}{\lambda}, \tag{2}$$

which assumes negligible clutter contamination of the target's interferogram. In the case of a non-negligible clutter contribution, the estimation of the target radial velocity from the contaminated interferometric phase may lead to erroneous results. The effect is most severe for dim, slowly moving targets, where the SCR and θ_t are small, and the targets become indistinguishable from the background clutter. As stated earlier, reducing the resolution cell areas reduces the clutter contribution to the target cell, which in turn helps to conserve the target's interferometric phase and correctly estimate its velocity. The SAR ATI is, therefore, a clutter-limited detector. On the other hand, reducing the clutter contribution does not benefit the SAR DPCA because the system noise, rather than the cancelled stationary clutter, limits the detector performance. This, of course, assumes that the system noise is the dominant interference over the clutter residues after the clutter cancellation.

Decorrelation model

For two-phase-centre DPCA, clutter-cancellation performance depends on several factors and is characterized by a single quantity, $1 - |\rho|$, called the decorrelation, where ρ is the correlation coefficient of the signals from fore and aft channels. Various decorrelation mechanisms are described here, most of which can be remedied using some suitable calibration techniques (Gierull, 2003). They are described here for a better understanding of the decorrelation mechanisms and are not to be taken as insurmountable limitations of the SAR DPCA approach. For the DPCA cancellation to work perfectly would require that the two virtual monostatic phase centres occupy the same point in space at times that differ by the DPCA processing lag. There are two sources of error that will induce an offset in the phase-centre locations. The antenna axis containing the transmit and two receive phase centres may be misaligned with the platform velocity (a yaw or pitch error). The result is a phase-centre offset that lies in the plane perpendicular to the platform velocity vector. The second mechanism is an error in the DPCA lag time, resulting in an offset along the velocity vector. Decorrelation of clutter returns can also be caused by the antenna deformation, which leads to the two receive beams illuminating the scene in a slightly different manner. Receiver channel mismatch can also be problematic, in that the channels may have different transfer functions. The transfer function includes the effect on the complex signal envelope of a chain of amplifiers and down-converters from the radio-frequency (RF) output of the receive beam combiner through to the input to the analog to digital (A/D) converter. Also, the receive beams, each independently formed from N array modules, may have uncompensated errors that differ randomly from module to module. It is also expected that, in the far sidelobes, the receive beam patterns will be uncorrelated. Therefore, there will be no cancellation of clutter received through these sidelobes. A/D conversion can also add to the overall noise. The fact that the ground clutter is not perfectly coherent because of internal motion will cause some degradation in DPCA performance. This may ultimately limit the system performance. The SBRMTISIM simulator, described in the next section, models some of these decorrelation mechanisms, such as channel mismatch, uncorrelated far sidelobes, A/D conversion noise, and clutter internal motion. The detailed modeling and descriptions of aforementioned decorrelation effects are found in Miller (1987). Here, we resort to a simple decorrelation model (I. Sikaneta, personal communication, 2004), which considers these effects as either an additive noise or a multiplicative random phase jitter θ.

For a two-channel SAR system, such as RADARSAT-2, one defines the column vector $z = [z_1\ z_2]^T$ with elements $z_1 = x_1 + n_1$

and $z_2 = x_2 + n_2$, where x_i represents stationary clutter signals from the ith channel, n_i is additive noise of the ith channel, and T is the transpose operator. The multiplicative random phase jitter that decorrelates channel 2 from channel 1 can be modeled as $x_2 = x_1 \exp(j\theta)$ assuming, for simplicity, that x_1 is deterministic and θ is normally distributed, i.e., $f_\theta(\theta) = N(0, \sigma_p^2)$. Then the expectation value of DPCA magnitude squared is

$$E\{|DPCA|^2\} = E\{(x_1 - x_2 + n_1 - n_2)*$$

$$\times (x_1 - x_2 + n_1 - n_2)\}, \qquad (3)$$

where * is the complex conjugate operator. Multiplying out Equation (3), the inner product of signal and noise terms all vanish except the following:

$$E\{|DPCA|^2\} = E\{|x_1|^2\} + E\{|x_2|^2\} - E\{x_1^* x_2\} - E\{x_2^* x_1\}$$

$$+ E\{|n_1|^2\} + E\{|n_2|^2\}. \qquad (4)$$

Substituting $x_1 \exp(j\theta)$ for x_2 in Equation (4), one gets

$$E\{|DPCA|^2\} = 2\xi_c^2 + 2\xi_n^2 - \xi_c^2 E\{\exp(j\theta)\}$$

$$-\xi_c^2 E\{\exp(-j\theta)\}, \qquad (5)$$

where $\xi_c^2 = E\{|x_i|^2\}$ and $\xi_n^2 = E\{|n_i|^2\}$, and the $E\{\exp(j\theta)\}$ terms can be shown to be equal to

$$E\{\exp(jt\theta)\} = \int_{-\infty}^{\infty} \frac{\exp(j\theta)\exp(-\theta^2/2\sigma_\theta^2)}{\sqrt{2\pi\sigma_\theta^2}} d\theta = \exp(-\sigma_\theta^2/2)$$

$$\times \int_{-\infty}^{\infty} \frac{\exp[-(\theta - j\sigma_\theta^2)^2/2\sigma_\theta^2]}{\sqrt{2\pi\sigma_\theta^2}} d\theta = \exp(-\sigma_\theta^2/2). \qquad (6)$$

Therefore, Equation (5) becomes

$$E\{|DPCA|^2\} = 2\xi_c^2[1 - \exp(-\sigma_\theta^2/2)] + 2\xi_n^2. \qquad (7)$$

Next, an expression is derived for the correlation coefficient ρ based on the decorrelation model given earlier. The covariance matrix of the two-channel SAR can be written as

$$\mathbf{R} = E\{zz^H\} = E\left\{ \begin{bmatrix} z_1^* z_1 & z_1^* z_2 \\ z_2^* z_1 & z_2^* z_2 \end{bmatrix} \right\}. \qquad (8)$$

Substituting for z_i and using the earlier results, one obtains

$$\mathbf{R} = \begin{bmatrix} E\{x_1^* x_1 + n_1^* n_1\} & E\{x_1^* x_2\} \\ E\{x_2^* x_1\} & E\{x_2^* x_2 + n_2^* n_2\} \end{bmatrix}$$

$$= \begin{bmatrix} \xi_c^2 + \xi_n^2 & \xi_c^2 \exp(-\sigma_\theta^2/2) \\ \xi_c^2 \exp(-\sigma_\theta^2/2) & \xi_c^2 + \xi_n^2 \end{bmatrix} \equiv \begin{bmatrix} \xi^2 & \xi^2\rho \\ \xi^2\rho & \xi^2 \end{bmatrix}. \qquad (9)$$

The correlation coefficient is therefore

$$\rho = \frac{\xi_c^2/\xi_n^2}{1 + \xi_c^2/\xi_n^2} \exp(-\sigma_\theta^2/2) = \frac{CNR}{1 + CNR} \exp(-\sigma_\theta^2/2), \qquad (10)$$

where CNR is the clutter-to-noise ratio. From Equation (10), ones notes that scene decorrelation depends on both the additive noise and the multiplicative phase jitter, but the ability of the DPCA to cancel clutter depends only on the multiplicative phase error, as can be seen from Equation (7). An additive noise, by itself, does not affect the ability of the DPCA to cancel clutter. This implies that the DPCA clutter-cancellation performance does not depend on the CNR if the additive noise is the only decorrelation mechanism present.

For RADARSAT-2, the CNR is about –10 dB lower than that of an airborne system such as the Canadian CV-580 (Livingstone et al., 2002) for similar SAR resolutions, clutter radar cross section (RCS), and noise temperatures. Therefore, the residual clutter for the RADARSAT-2 is expected to be less of a problem than the system noise in terms of limiting the RADARSAT-2 DPCA performance. From anticipated RADARSAT-2 noise temperatures and simulation data (EMS Technologies and MacDonald Dettwiler and Associates, 2002), one assumes, in the following analysis, that DPCA clutter cancellation is effective and that the remaining clutter residue, due to multiplicative phase errors, is small compared with the overall system noise. The SAR DPCA detection performance can then be said to be noise-limited. On the other hand, the SAR ATI performance is assumed to be clutter-limited because the interferometric phase is the detection metric used in the SAR ATI and is usually corrupted by the overlapping clutter. It is within this context that the performance of the two processing approaches is examined and predicted from the following radar equation analysis.

Radar equation analysis

After the SAR processing of N_r range samples and N_a azimuth samples (of an aperture), the radar equations for point target power P_t, clutter power P_c, and noise power P_n are as follows:

$$P_t = (N_r N_a)^2 \frac{P_T G_T G_R \lambda^2 \sigma_t}{(4\pi)^3 R^4} \qquad (11)$$

$$P_c = (N_r N_a)^2 \frac{P_T G_T G_R \lambda^2 \sigma_c^0 \rho_r \rho_a}{(4\pi)^3 R^4} \qquad (12)$$

$$P_n = (N_r N_a) k_B T B \qquad (13)$$

where G_T and G_R are the transmit and receive antenna gains, respectively; σ_t and σ_c^0 are the target RCS and clutter-normalized RCS, respectively; ρ_r and ρ_a are the range and azimuth resolutions, respectively; P_T is the peak transmitted power; k_B is the Boltzmann constant; T is the temperature; B is the receiver bandwidth; λ is the wavelength; and R is the slant range (Franceschetti and Lanari, 1999). Both the target power and the clutter power increase as $(N_r N_a)^2$ because the samples are summed coherently. The noise power, on the other hand, increases as $N_r N_a$ because the samples are summed incoherently. The target signal-to-noise ratio (SNR) as a function of the bandwidth can be shown to be

$$SNR = \frac{P_t}{P_n} = \frac{N_r N_a}{B} \aleph_t = \frac{(B\tau)(\lambda R f_p / 2 v_s \rho_a)}{B} \aleph_t \propto \frac{1}{\rho_a}, \qquad (14)$$

where $\aleph_t = P_T G_T G_R \lambda^2 \sigma_t / [(4\pi)^3 R^4 k_B T]$ contains the bandwidth-independent terms; $N_a = \lambda R f_p / 2 v_s \rho_a$; f_p is the pulse repetition frequency; and v_s is the platform velocity (Curlander and McDonough, 1991; Franceschetti and Lanari, 1999). It is also assumed that the sampling rate $f_s \geq B$ and $N_r \approx B\tau$, the anti-aliasing condition (where τ is the pulse width). Therefore, the SNR for a point target is independent of the processing bandwidth B or the range resolution ρ_r but inversely proportional to the azimuth resolution ρ_a. This implies that increasing the signal bandwidth or the slant-range resolution would not benefit a noise-limited detector such as the DPCA. On the other hand, the SCR can be shown to be

$$SCR = \frac{P_t}{P_c} = \frac{\sigma_t}{\sigma_c^0 \rho_a \rho_r} = \frac{\sigma_t}{\sigma_c^0 \rho_a} \frac{2B \sin \eta}{c}, \qquad (15)$$

where $\rho_r = c / (2B \sin \eta)$, and η is the incidence angle (Franceschetti and Lanari, 1999). In contrast to the SNR, the SCR is a function of both range and azimuth resolutions and is directly proportional to the processing bandwidth B. Since the SAR ATI is a clutter-limited detector for slowly moving targets, an increase in the bandwidth B (or the range resolution) is expected to favor the SAR ATI over the SAR DPCA. Likewise, the CNR can be shown to be

$$CNR = \frac{P_c}{P_n} = \frac{N_r N_a \rho_r \rho_a}{B} \aleph_c$$

$$= \frac{(B\tau)[\lambda R f_p / (2 v_s \rho_a)][c / (2B \sin \eta)] \rho_a}{B} \aleph_c$$

$$= \frac{\tau \lambda R f_p c}{4 v_s \sin \eta} \frac{\aleph_c}{B}, \qquad (16)$$

where $\aleph_c = P_T G_T G_R \lambda^2 \sigma_c^0 / [(4\pi)^3 R^4 k_B T]$, indicating that the CNR is inversely proportional to the bandwidth B or

Table 2. SNR, SCR, and CNR dependencies on SAR resolutions.

Ratio	SAR resolution (ρ_r, ρ_a) or bandwidth B
SNR	Independent of ρ_r or B; $\propto 1/\rho_a$
SCR	$\propto 1/\rho_r$ or $\propto B$; $\propto 1/\rho_a$
CNR	$\propto \rho_r$ or $\propto 1/B$; independent of ρ_a

proportional to ρ_r, but independent of ρ_a (Curlander and McDonough, 1991; Franceschetti and Lanari, 1999). **Table 2** summarizes the results of this analysis. Since the SAR DPCA detection is noise-limited (for negligible clutter residues) and the SNR remains constant with the bandwidth, the performance is expected to be poorer (i.e., fewer detections) at finer range resolutions if the number of false alarms, N_{FA} (= $N_r N_a P_{FA}$, where P_{FA} is the false alarm probability), is kept constant. The previous predictions are tested against simulation data in the following sections. It should also be noted that, in the SAR ATI, the noise tends to scatter the clutter signal around zero phase and therefore may also obscure targets with smaller interferometric phase angles.

Simulation

SBRMTISIM simulator

The simulated results described in this study are obtained using a space-based moving target indication (MTI) radar simulator known as the SBRMTISIM, developed by Sicom Systems Ltd. (Nohara et al., 1999) for the Canadian Department of National Defence (DND). The simulator provides an environment definition window that allows the user to specify the look geometry and define clutter regions and targets to create a scenario. Clutter is modeled as a dense set of regularly distributed scatterers (many scattering centres per resolution cell) with user-specified cross section, scattering statistics, and internal motion. Targets are modeled as point scatterers with user-specified velocity, cross section, and fading statistics. Other windows are used to specify the radar and antenna parameters and other parameters needed to characterize the system. Once these parameters are specified, the simulator generates high-fidelity, complex, base-band signals representing the signals received by the space-based radar (SBR). The complete, two-way path of the signal is modeled from the transmitter, to the earth, and back to the receiver.

Experimental definition

The simulation experiments are carried out in three RADARSAT-2 signal bandwidths, namely 12, 50, and 100 MHz, which yield ground range resolutions of 25, 6, and 3 m, respectively, at a 30° incidence angle. The 100 MHz bandwidth is not supported by the RADARSAT-2 MODEX mode but has been simulated to emphasize the effect of range resolution on the performance of the two detection schemes (DPCA and ATI). The radar parameters used in the simulations
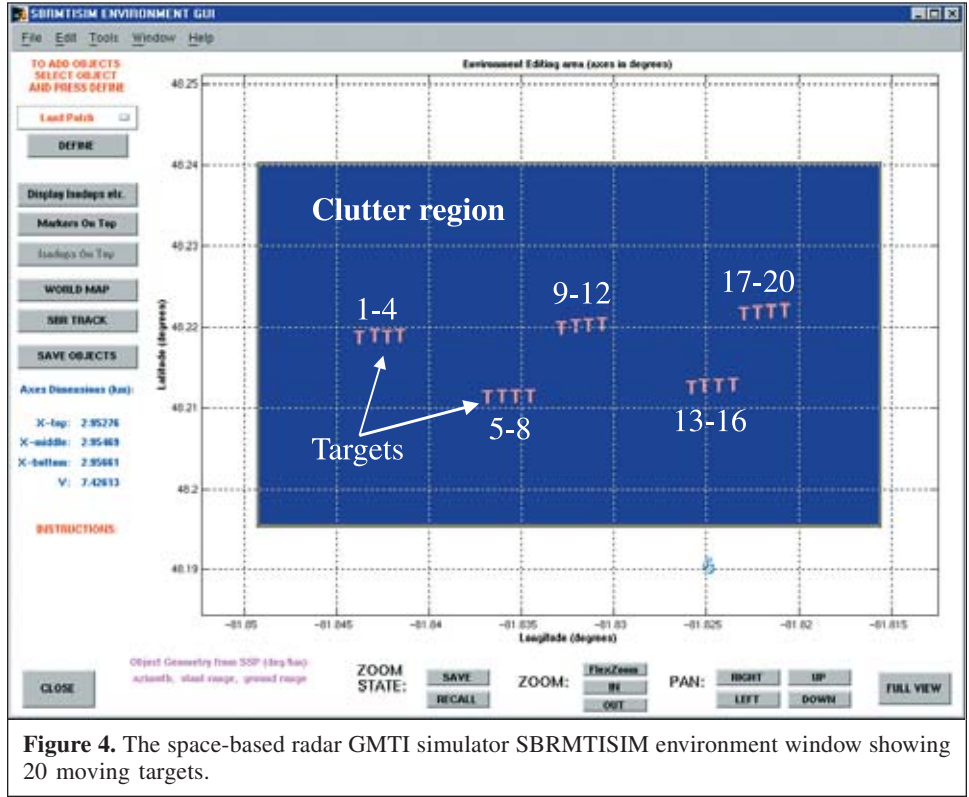
Figure 4. The space-based radar GMTI simulator SBRMTISIM environment window showing 20 moving targets.

Table 3. Radar system parameters.

Peak power (W)	2400
Carrier frequency (GHz)	5.4
Pulse width (µs)	42
Pulse bandwidth (MHz)	12, 50, 100
Slant-range resolution (m)	12.5, 3, 1.5
Azimuth resolution (m)	25
Burst length (s)	0.75
Intermediate-frequency (IF) bandwidth (MHz)	14.4, 60, 120
A/D sampling rate (MHz)	15.2, 63.4, 126.7
IF filter type	Butterworth
Channel to channel mismatch (dB)	–50
No. of A/D bits	8
Radar system loss (dB)	0
Noise temperature (K)	795.11
PRF (Hz)	1988.3
Waveform	LFM
Model receiver	Yes
IF centre frequency (MHz)	1013
IF filter order	8
A/D quantization level	–100
No. of mismatch ripples	4

Table 4. Land clutter characteristics.

Range swath (km)	1.5
Clutter patch (km × km)	2.5 × 5.0
Type (land or sea)	Land
Centre longitude (°)	–81.8324
Centre latitude (°)	48.2178
Longitude size (km)	2.5
Latitude size (km)	5
Along-range scatterer spacing (m)	2
Cross-range scatterer spacing (m)	4
Clutter amplitude distribution	Raleigh
Clutter phase distribution	Uniform
Mean clutter cross section (m^2/m^2)	0.1 (–10 dB)
Clutter internal motion (m/s)	0.1
Incidence angle (°)	30

are summarized in **Table 3**. For all scenarios examined, the azimuth resolution is kept constant at 25 m, which is the specified azimuth resolution for the RADARSAT-2 standard beam. This leads to an unreasonable 8:1 aspect ratio at 100 MHz bandwidth but is used purposely so that one can exclusively examine the effect of bandwidth changes on the

processor performance. In this study, no simulation runs are carried out to examine the effect of azimuth resolution ρ_a on the detector performance.

For all simulation runs, a targets-plus-a-clutter scene (**Figure 4**) is simulated with a 1.5 km range swath, which contains a 2.5 km × 5.0 km land clutter patch with a reflectivity of –10 dB m^2/m^2 and a spectral width of 0.1 m/s. Scene texture elements (inhomogeneous clutter) are not introduced into the model so that the DPCA process can be tested under ideal conditions. It is noted that the SAR ATI is less sensitive to scene inhomogeneity than the SAR DPCA (Livingstone et al., 2002). The clutter amplitudes are Rayleigh distributed, the clutter phase is uniformly distributed, and the land patch is statistically uniform. The land patch characteristics used in the

Table 5. Target parameters.

Target No.	Scenario 1 RCS (m²)	Ground speed (km/h)	Scenario 2 RCS (m²)	Ground speed (km/h)	Scenario 3 RCS (m²)	Ground speed (km/h)	Scenario 4 RCS (m²)	Ground speed (km/h)
1	45	54 (east)	45	24 (east)	45	130 (east)	35	20 (east)
2	45	36 (east)	45	21 (east)	45	120 (east)		
3	45	18 (east)	45	18 (east)	45	110 (east)		
4	45	12 (east)	45	15 (east)	45	100 (east)		
5	40	54 (west)	40	24 (west)	40	130 (west)		
6	40	36 (west)	40	21 (west)	40	120 (west)		
7	40	18 (west)	40	18 (west)	40	110 (west)		
8	40	12 (west)	40	15 (west)	40	100 (west)		
9	35	54 (east)	35	24 (east)	35	130 (east)		
10	35	36 (east)	35	21 (east)	35	120 (east)		
11	35	18 (east)	35	18 (east)	35	110 (east)		
12	35	12 (east)	35	15 (east)	35	100 (east)		
13	30	54 (west)	30	24 (west)	30	130 (west)		
14	30	36 (west)	30	21 (west)	30	120 (west)		
15	30	18 (west)	30	18 (west)	30	110 (west)		
16	30	12 (west)	30	15 (west)	30	100 (west)		
17	20	54 (east)	20	24 (east)	20	130 (east)		
18	20	36 (east)	20	21 (east)	20	120 (east)		
19	20	18 (east)	20	18 (east)	20	110 (east)		
20	20	12 (east)	20	15 (east)	20	100 (east)		

simulations, summarized in **Table 4**, are the same for all three bandwidths investigated. The satellite heading is approximately north (i.e., 98.6° inclination) with right-looking geometry.

Four target scenarios with different target RCS and velocity parameter sets (**Table 5**) are constructed and are exercised in 75 simulation runs. Twenty targets (except scenario 4), moving either eastward or westward, are generated within the simulated land surface. The approximate initial positions of the targets in the land patch are shown in **Figure 4**, and their average slant range and ground range are 1034.21 m (±0.82 m) and 627.53 m (±1.21 m), respectively. The average elevation (or look) angle is 37.286° (±0.049°) and the average azimuth squint angle is 2.826° (±0.011°). The first scenario simulates targets with ground speeds ranging from 12 to 54 km/h. The 14–24 km/h speed range chosen for scenario 2 provides detail in the vicinity of the 20 km/h target speed where scenario 1 results indicate the largest performance difference between the two processing approaches. The third scenario simulates high-speed targets (100–130 km/h) to investigate the performance of the two processors when there is a significant mismatch between the SAR terrain-matched filter and the moving targets. The targets are positioned in the same land patch as in the two previous scenarios but their initial positions are adjusted to retain the Doppler shifted target images within the modeled terrain patch. The fourth scenario simulates only a single moving target in a clutter background to visually examine the performance of the two processing approaches as a function of the processing bandwidth (or range resolution). All generated radar signals are processed in both the SAR DPCA and the SAR ATI architectures.

Results and discussion

Scenario 1

When plotting the complex interferogram of the SAR ATI output as a function of its magnitude and phase, a bell-shaped distribution results (see **Figure 5A** for the scenario 1 and 12 MHz bandwidth simulation run). Applying the nonparametric CFAR detection scheme, described in Chiu (2002; 2005), to the result using contour lines as detection-threshold functions (see **Figure 5B**), one obtains a GMTI image as plotted in **Figure 6**, showing 12 detected targets and 13 false alarms, for a false alarm probability P_{FA} of ~2 × 10⁻⁴. Similarly, when the SAR DPCA output signal is plotted in the complex plane, as shown in **Figure 2**, the clutter signal is suppressed to a noise "disk" about the origin, and moving targets with sufficiently large SNR appear above the noise floor. Passing the SAR DPCA output through a cell-averaging constant false alarm rate (CA-CFAR) detector (Skolnik, 1990), with P_{FA} set at 2 × 10⁻⁴, results in a GMTI image similar to that of the SAR ATI (**Figure 6**), also with 12 detected targets but only 11 false alarms. When averaged over four simulation runs with different signal-generation seeds, there is essentially no difference in the number of targets detected by the two processing approaches at this bandwidth (or range resolution); both methods detect an average of 14 out of 20 moving targets (**Table 6**). Therefore, the SAR DPCA and SAR ATI have about the same GMTI performance when the bandwidth is 12 MHz. One should note that the performance of the two detection schemes is very much dependent on system noise and clutter levels. Therefore, the comparison is only valid for the noise and clutter levels
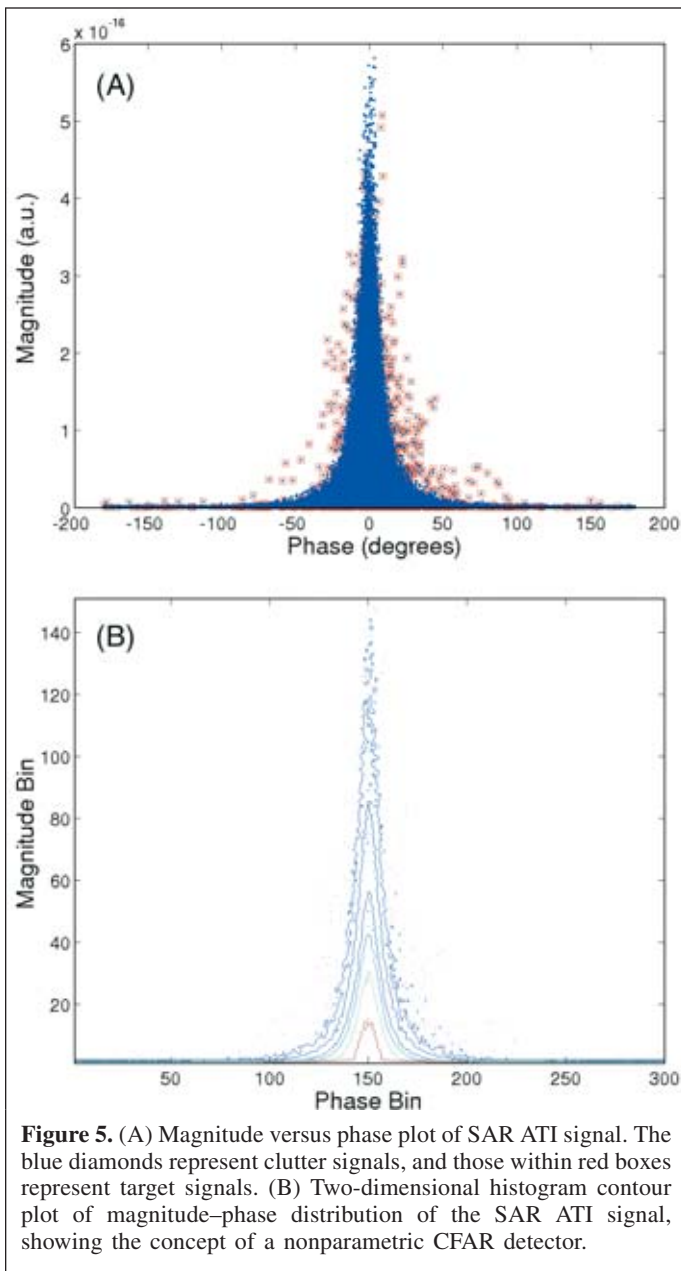
Figure 5. (A) Magnitude versus phase plot of SAR ATI signal. The blue diamonds represent clutter signals, and those within red boxes represent target signals. (B) Two-dimensional histogram contour plot of magnitude–phase distribution of the SAR ATI signal, showing the concept of a nonparametric CFAR detector.

expected for RADARSAT-2-class radars. Thus, the following results must be understood and interpreted within this context. Nevertheless, it is expected that reducing the system noise favors the SAR DPCA, because of its noise-limited performance, in the same way that increasing the SAR resolution benefits the SAR ATI. This, however, can only be confirmed from a more detailed simulation study.

The 50 and 100 MHz cases for scenario 1 are also generated and the signals processed. When averaged over four simulation runs and rounded to the nearest integer, 13 and 12 targets are detected by the SAR DPCA at 50 and 100 MHz bandwidths, respectively, compared with 14 and 15 targets detected by the SAR ATI at the same bandwidths (see **Table 6**). These are obtained by keeping the number of false alarms, N_{FA}, approximately constant, i.e., by using P_{FA} values of 2.0×10^{-4},

4.3×10^{-5}, and 2.5×10^{-5} for 12, 50, and 100 MHz, respectively. Also plotted in **Figure 7A** are the results before rounding to the nearest integer, with error bars representing standard deviations in the four simulation runs. The SAR ATI performance improves with increasing bandwidth, whereas the SAR DPCA deteriorates under the same conditions.

Scenario 2

The results from scenario 1 show that the targets with velocities in the vicinity of 20 km/h are of particular interest because they are often detected by the SAR ATI but missed by the SAR DPCA at higher bandwidths (or finer range resolutions). To highlight the difference observed in the performance of the two detectors, we choose a target speed range of 15–24 km/h for scenario 2. The results from the three bandwidth cases show the difference between the processors' performance is indeed emphasized. At a bandwidth of 12 MHz, 12 and 11 targets are detected by the SAR DPCA and SAR ATI, respectively. At higher bandwidths, however, only 10 (50 MHz) and eight (100 MHz) targets are detected by the SAR DPCA compared with 15 (50 MHz) and 16 (100 MHz) by the SAR ATI (see **Table 6**; **Figure 7B**). Therefore, for scenario 2 and a bandwidth of 100 MHz, the SAR ATI outperforms the SAR DPCA in all cases examined by about 50%. The results are consistent with those predicted by the radar equation analysis.

Scenario 3

When a stationary terrain-matched filter is used on high-speed targets (scenario 3), the two processing approaches show similar GMTI performance, with the SAR DPCA displaying a slight edge over the SAR ATI. The SAR DPCA detects 12, 12, and 11 targets at 12, 50, and 100 MHz bandwidths, respectively, whereas the SAR ATI detects 10, 11, and 9 targets at the same resolutions. Both detectors miss most of the 130 km/h targets, and only a few 120 km/h targets are detected. On the other hand, most of the 100 km/h targets are detected. Both detectors show a slight decline in the performance with increasing bandwidth when the number of false alarms is kept relatively constant. The results for the high-speed targets are also summarized in **Table 6** and plotted in **Figure 7C**. Note that there is no improvement in the SAR ATI processor performance with increasing bandwidth, in direct contrast with the previous low-speed cases. The reason for this is that the stationary clutter is centred around zero phase and therefore the SAR ATI is only clutter-limited for low-speed targets (small phase angles). For the high-speed targets, however, the SAR ATI becomes noise-limited, as there are no clutter signals with large phase angles. Because of an increasing mismatch between the terrain-matched filter and the moving targets, the targets with very high radial speeds are severely attenuated and less likely to be detected. Range cell migrations also become increasingly more severe as the target radial speed increases. For a 3 m ground range resolution, a 60 km/h target moves through two range cells within the maximum available integration time, and a 130 km/h target moves through as many as four range cells. The

Table 6. Summary of the performance of two processors (number of targets detected).

Bandwidth (MHz)	Matched filter radial velocity offset							
	0 km/h		20 km/h		50 km/h		–50 km/h	
	ATI	DPCA	ATI	DPCA	ATI	DPCA	ATI	DPCA
Scenario 1								
12	14±2 (22)	14±1 (20)	12±3	12±2				
50	14±1 (30)	13±2 (27)	14±2	12±2				
100	15±1 (25)	12±1 (26)	14±2	12±1				
Scenario 2								
12	11±3 (19)	12±2 (16)	11±3	11±2				
50	15±2 (22)	10±1 (20)	14±2	11±3				
100	16±3 (21)	8±1 (23)	16±2	6±2	15±2	7±2	14±2	7±2
Scenario 3								
12	10±2 (12)	12±2 (12)	11±1	12±1				
50	11±1 (12)	12±1 (13)	11±1	12±1				
100	9±2 (16)	11±1 (10)	10±1	12±1	12±0	12±0	8±0	8±0

Note: Number of targets detected averaged over four simulation runs. The average number of false alarms is given in parentheses.
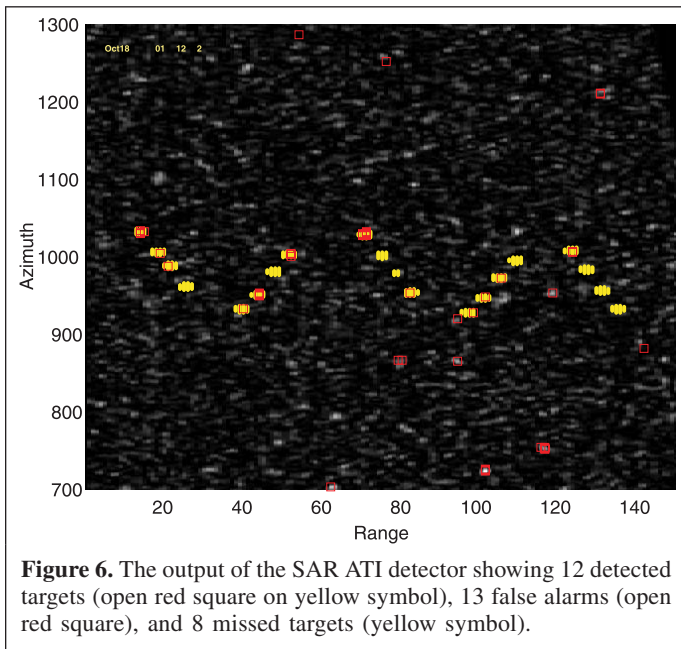

Figure 6. The output of the SAR ATI detector showing 12 detected targets (open red square on yellow symbol), 13 false alarms (open red square), and 8 missed targets (yellow symbol).
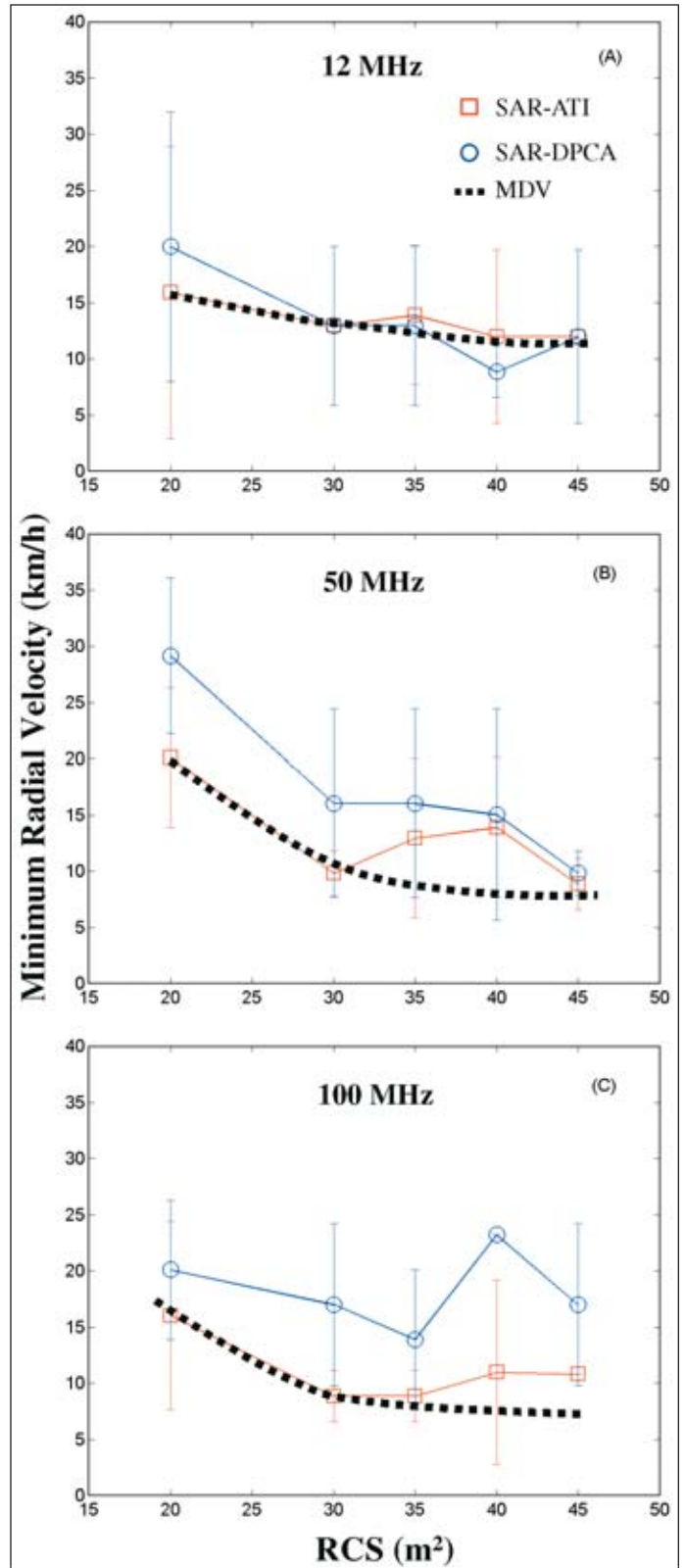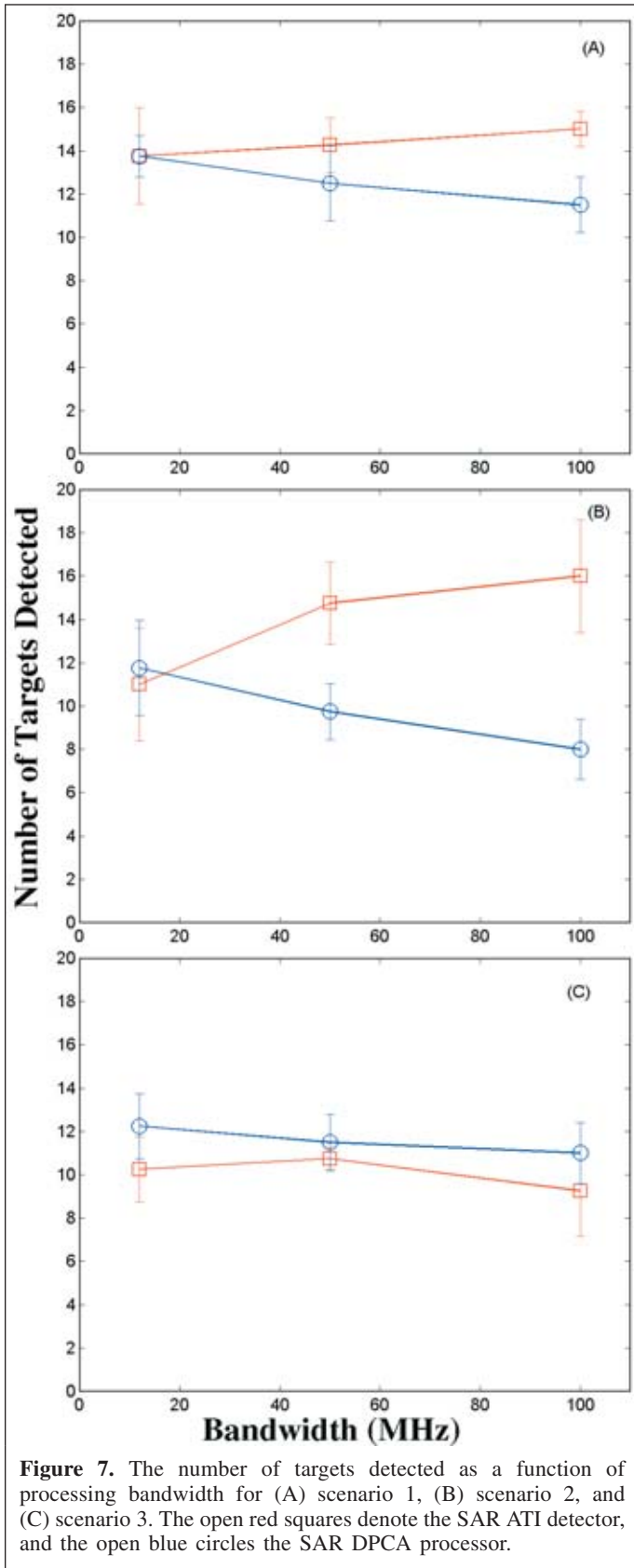
energy spread across the cells reduces the target signal strength and smears the target image. With severely attenuated signals, the SAR ATI becomes noise-limited at large interferometric phase angles, and therefore its performance is not expected to improve with increasing bandwidth as in the low-speed cases where the detector is limited by the clutter.

The results given here are obtained by processing the SAR data with a stationary-world assumption, which leads to significant defocusing and attenuation of the moving targets but a focused stationary background. For fast movers, a motion-addressed matched filter (Livingstone et al., 2002) can be designed to better track the velocity and acceleration of a target. As a first approximation, a constant radial velocity may be used to represent the motion of the target, since the simulated targets are moving either towards or away from the radar. A motion-matched filter will not only provide a first estimate of the radial

speed of the target but also complement coherent velocity estimation by gathering the energy of the target into a more cohesive, cleaner cluster of points, thus improving the SCR and the SNR and allowing fast-moving targets to be more easily extracted. Therefore, when the high-velocity cases are reprocessed with a +50 km/h radial velocity offset matched filter (or +100 km/h ground speed at 30° incidence), both processors detect all the east-moving targets but miss all the west-moving ones. The opposite is true when the data are processed with the –50 km/h matched filter (see also **Table 6**). As expected, the radial velocity offset of ±50 km/h (±100 km/h ground), which closely matches the ±100–130 km/h targets but significantly mismatches the stationary world, leads to detection of all sign-matched moving targets by both the SAR ATI and the SAR DPCA because of the improved SCR and SNR. In this case, the processors perform identically.

Minimum detectable velocity (MDV) and bandwidth

The minimum radial velocities (MRVs) that are detected by the two processors as a function of target RCS are also examined, and the results are plotted in **Figure 8**. The MRVs are averaged over four simulation runs. The error bars represent the standard deviations in the four runs. For an RCS of say 30 m^2, the minimum detectable radial velocities (MDRV) are predicted, for the RADARSAT-2 type sensor, to be 13, 16, and 18 km/h for the SAR DPCA and 13, 10, and 9 km/h for the SAR ATI at 12, 50, and 100 MHz, respectively. As can be seen in **Figure 8**, the MDRV increases with increasing bandwidth for the SAR DPCA but decreases for the SAR ATI. At higher bandwidths, 50 and 100 MHz, the SAR ATI has MDRVs that are consistently lower than those of the SAR DPCA. This is in agreement with the observed performance of the two processors with respect to the range resolution. Also shown in **Figure 8** are MDRV values (broken lines) as a function of RCS evaluated from the SAR ATI detection-threshold functions (i.e., the contour lines that represent the detection thresholds; see **Figure 5B**) used in the 12, 50, and 100 MHz bandwidths,
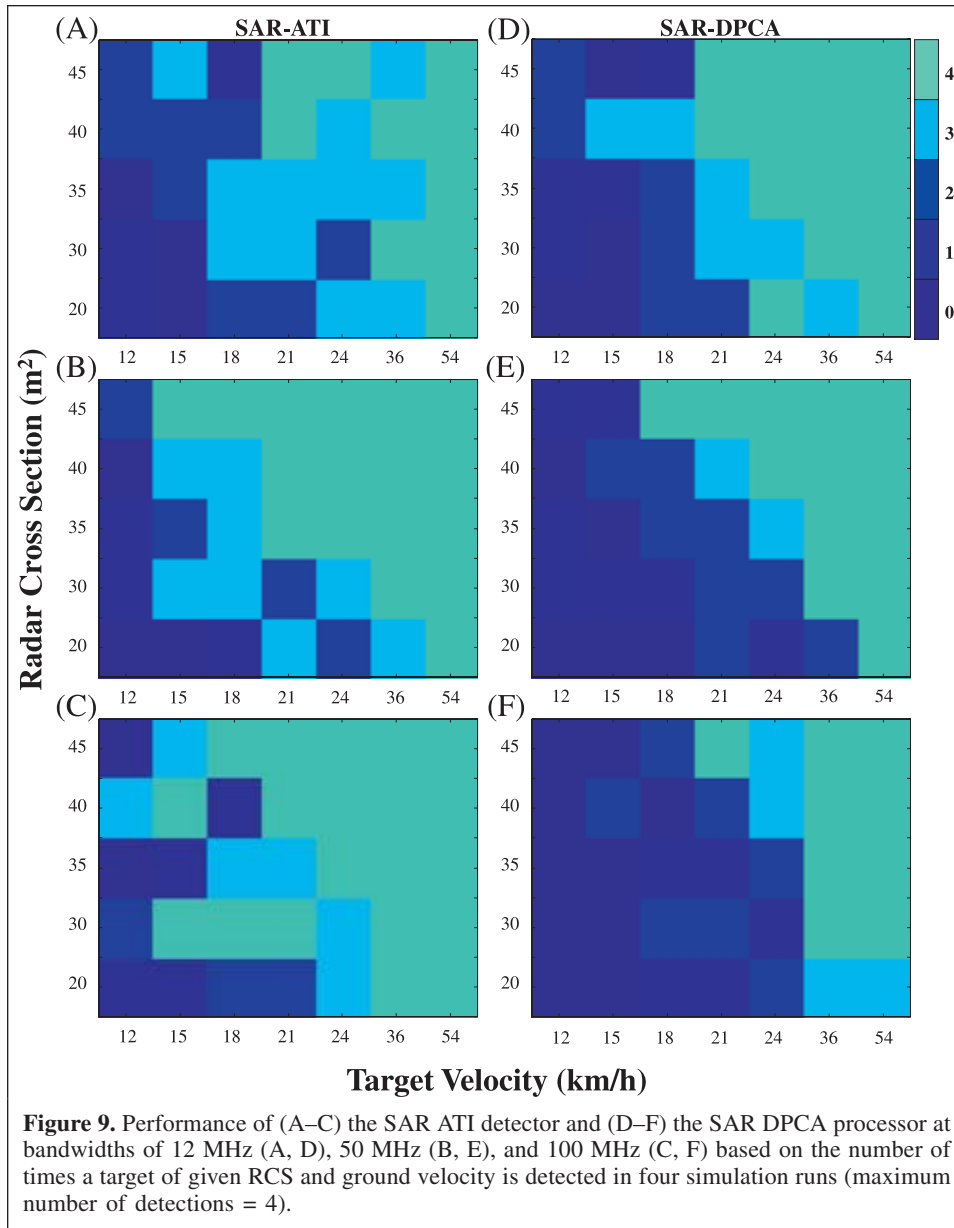
Figure 7. The number of targets detected as a function of processing bandwidth for (A) scenario 1, (B) scenario 2, and (C) scenario 3. The open red squares denote the SAR ATI detector, and the open blue circles the SAR DPCA processor.

Figure 8. Minimum target radial velocity detected as a function of RCS averaged over four simulation runs for bandwidths of (A) 12 MHz, (B) 50 MHz, and (C) 100 MHz. The open red squares denote the SAR ATI, the open blue circles the SAR DPCA, and the broken lines the minimum detectable velocity (MDV) derived from threshold functions of the nonparametric CFAR detector (Chiu, 2005).

respectively. The chosen contour line forms the boundary between the stationary world and the moving targets, and ATI phase θ_t as a function of ATI magnitude ξ, represented by the contour line, is the minimum radial velocity ($\propto \theta_t$) as a function of target RCS ($\propto \xi$) that can be detected by the ATI detector for a given false alarm rate. RCS values are calculated from the magnitude of the interferogram ξ, taking into account the attenuation factors such as target-velocity mismatch and antenna modulation. These computed values do not take into account the target–clutter interference effect mentioned earlier. Therefore, the discrepancy between the calculated and experimental (or simulated) values for small radial velocities (see **Figure 8**) may be attributed to the target–clutter interference, since the effect is expected to be most severe at small phase angles where target and clutter are barely distinguishable.

The performance of the two processors is also presented in a different format in **Figure 9**, which shows the number of times a target of given RCS and ground velocity is detected in four different simulation runs at the three processing bandwidths. The results show the performance improvement in the SAR ATI, but not in the SAR DPCA, with increasing bandwidth for a constant number of false alarms. At 12 MHz, the SAR ATI appears to perform poorer than the SAR DPCA for targets with larger RCSs and velocities but better than the SAR DPCA for targets with smaller RCSs and velocities. For higher bandwidths, however, the SAR ATI is consistently better than the SAR DPCA for almost all RCS–velocity combinations.

Scenario 4

To demonstrate visually the performance dependence of the two processing approaches on the processing bandwidth (or

Figure 9. Performance of (A–C) the SAR ATI detector and (D–F) the SAR DPCA processor at bandwidths of 12 MHz (A, D), 50 MHz (B, E), and 100 MHz (C, F) based on the number of times a target of given RCS and ground velocity is detected in four simulation runs (maximum number of detections = 4).

range resolution), a fourth scenario is simulated using only a single target moving in a clutter background. A target speed of 20 km/h and an RCS of 35 m^2 are chosen so that the target is barely detectable by the two processors using the standard beam mode (12 MHz). The clutter statistics are the same as those used in the first three scenarios. Radar signals are generated for the three signal bandwidths (i.e., 12, 50, and 100 MHz). The generated signals are processed using the two SAR GMTI approaches (**Figure 1**), and the results are shown in

Figure 10. It should be noted that all SAR outputs are scaled by a constant noise power. That is, an increase in SNR is represented as an increase in signal relative to a constant noise source.

For SAR ATI processed signals, the SCR is clearly seen to improve with the increasing bandwidth, as predicted by the radar equation analysis. The target is barely detectable at 12 and 50 MHz bandwidths but is completely clear of the clutter at 100 MHz because of a reduced clutter contribution. The SAR
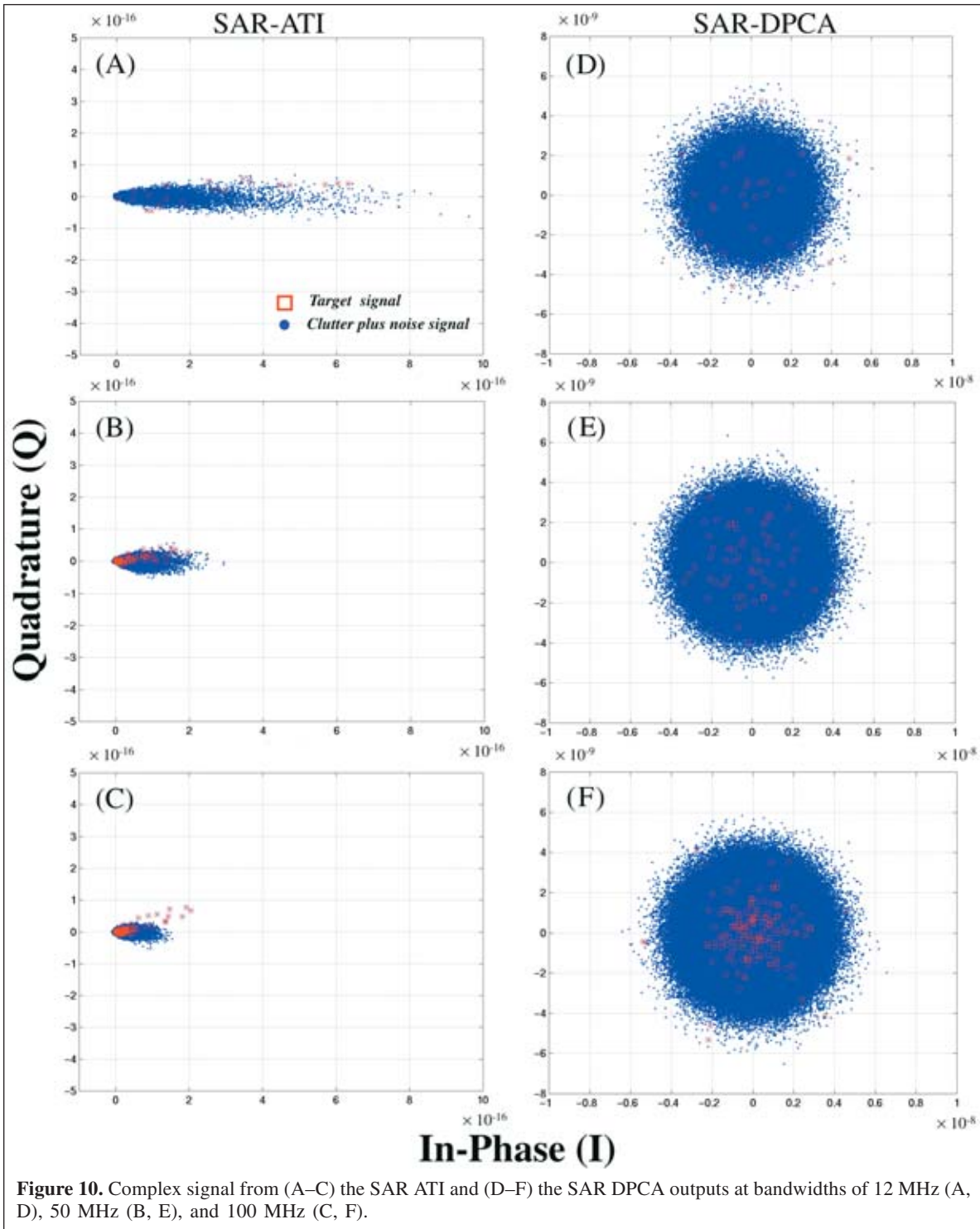

Figure 10. Complex signal from (A–C) the SAR ATI and (D–F) the SAR DPCA outputs at bandwidths of 12 MHz (A, D), 50 MHz (B, E), and 100 MHz (C, F).

DPCA approach, on the other hand, shows no noticeable improvement in the SNR as the bandwidth increases.

The results indicate that, when the bandwidth is increased, the performance of the SAR DPCA processor remains the same in terms of the SNR but deteriorates in terms of the number of detections (N_D) at a constant number of false alarms (N_{FA}). On the other hand, the performance of the SAR ATI improves in terms of the SCR with the increasing bandwidth. Thus, the SAR ATI is clearly a better detector compared to the SAR DPCA for low-speed cases at high bandwidths.

Conclusions

Two of the GMTI processing approaches currently being considered for Canada's RADARSAT-2 MODEX mode are examined. One makes use of the DPCA clutter-cancellation technique to provide subclutter visibility for dim moving objects. The other is based on the along-track SAR interferometry technique, in which magnitude and phase information of the targets' interferograms are exploited to allow their extraction from the clutter background. The performance of each processor is examined for three RADARSAT-2 range resolution modes. The study focuses on the influence of SAR resolution on the processor performance. For the 12 MHz case, the two methods display equivalent performance. At high SAR range resolutions, however, the results clearly demonstrate that the SAR ATI processor performs better than the SAR DPCA in its ability to detect slowly moving targets. The reason for the observed difference between the processor performances is the improvement in the SCR but not in the SNR as the SAR range resolution is increased. This is confirmed by both analysis and simulation. This directly affects the performance of the processor, which is shown to be clutter-limited for the SAR ATI and noise-limited for the SAR DPCA. The performance of the two processors is also evaluated for high-speed targets (>100 km/h). Unlike the low-speed cases, the processors do not show a difference in their performance when a velocity-offset matched filter is used. For RADARSAT-2 MODEX, it is likely that the difference between the two GMTI processing techniques due to the improvement in the SCR at high-resolution modes will not be as pronounced as that shown in this simulation study because the MODEX mode can only be operated at a maximum bandwidth of 50 MHz. Nevertheless, it is recommended that the SAR ATI be used rather than the SAR DPCA for higher SAR resolutions based on the current result. The two approaches could complement each other, however, in different clutter–noise scenarios and should be used concurrently.

Acknowledgements

References

Chiu, S. 2000a. *An analysis of RADARSAT-2 SAR-GMTI performance for standard beam mode*. Defence Research Establishment Ottawa (DREO), Technical Report TR 2000-088.

Chiu, S. 2000b. *Performance of RADARSAT-2 SAR-GMTI processor at high SAR resolutions*. Defence Research Establishment Ottawa (DREO), Technical Report TR 2000-093.

Chiu, S. 2002. SAR along-track interferometry with application to RADARSAT-2 ground moving target indication. In *SPIE Conference on Image and Signal Processing*, 24–27 September 2002, Crete, Greece. Edited by S.B. Serpico. International Society for Optical Engineering, Bellingham, Wash. Proceedings of SPIE, Vol. 4885, pp. 246–255.

Chiu, S. 2003. Clutter effects on ground moving target velocity estimation with SAR along-track interferometry. In *IGARSS'2003, Proceedings of the International Geoscience and Remote Sensing Symposium*, 21–25 July 2003, Toulouse, France. IEEE, New York. [CD-ROM].

Chiu, S. 2005. A constant false alarm rate (CFAR) detector for RADARSAT-2 along-track interferometry. *Canadian Journal of Remote Sensing*, Vol. 31, No. 1, pp. 73–84.

Coe, D.J., and White, R.G. 1995. Moving target detection in SAR imagery: experimental results. In *Proceedings of the IEEE International Radar Conference*, 8–11 May 1995, Alexandria, Va. IEEE, New York. pp. 644–649.

Curlander, J.C., and McDonough, R.N. 1991. *Synthetic aperture radar: systems and signal processing*. Wiley-Interscience, New York. pp. 123–124.

Dickey, F.R., Jr., and Santa, M.M. 1953. *Final report on anticlutter techniques*. General Electric Company, Report R65EMH37.

EMS Technologies and MacDonald Dettwiler and Associates. 2002. *RADARSAT-2 SAR payload, critical design review (CDR), March 11–15, 2002*. EMS Technologies and MacDonald Dettwiler and Associates, Richmond, B.C.

Ender, J.H.G. 1999. Space–time processing for multi-channel synthetic aperture radar. *Electronics & Communication Engineering Journal*, Vol. 11, pp. 29–38.

Erwin, S.I. 2001. Airborne radar: military systems redesigned for commercial applications. *National Defence Magazine*, August 2001. Available at http://www.nationaldefensemagazine.org/issues/2001/Aug/Airborne_Radar.htm.

Franceschetti, G., and Lanari, R. 1999. *Synthetic aperture radar processing*. CRC Press, Boca Raton, Fla. Sect. 1.10, pp. 60–61.

Gierull, C.E. 2002a. Statistics of multilook SAR interferograms for CFAR detection of ground moving targets. In *Proceedings of the 4th European Conference on Synthetic Aperture Radar (EUSAR)*, 4–6 June 2002, Cologne, Germany. VDE Verlag GmBH, Berlin. pp. 625–628.

Gierull, C.H. 2002b. Moving target detection with along-track SAR interferometry. Defence Research Establishment Ottawa (DREO), Technical Report TR 2002-084.

Gierull, C.H. 2003. Digital channel balancing of along-track interferometric SAR data. Defence Research Establishment Ottawa (DREO), Technical Memorandum TM 2003-024.

Goldstein, R.M., and Zebker, H.A. 1987. Interferometric radar measurements of ocean currents. *Nature (London)*, Vol. 328, pp. 707–799.

Livingstone, C.E. 1998. The addition of MTI modes to commercial SAR satellites. In *Proceedings of the 10th CASI Conference on Astronautics*, 26–28 Oct. 1998, Ottawa, Ont. Canadian Aeronautics and Space Institute, Ottawa, Ont. pp. 267–275.

Livingstone, C.E., Sikaneta, I., Gierull, C.H., Chiu, S., Beaudoin, A., Campbell, J., Beaudoin, J., Gong, S., and Knight, T.A. 2002. An airborne synthetic aperture radar (SAR) experiment to support RADARSAT-2 ground moving target indication (GMTI). *Canadian Journal of Remote Sensing*, Vol. 28, No. 6, pp. 794–813.

Luscombe, A. 1995. The Radarsat Project. *IEEE Canadian Review*, Fall 1995, No. 21.

Miller, R.W. 1987. *Radar requirements for DPCA clutter cancellation*. Massachusetts Institute of Technology, Lincoln Laboratory, Project Report SRT-27.

Moccia, A., and Rufino, G. 2001. Spaceborne along-track SAR interferometry: performance analysis and mission scenarios. *IEEE Transactions on Aerospace and Electronic Systems*, Vol. 37, No. 1, pp. 199–213.

Nohara, T.J., Premji, A., and Weber, P. 1999. *Final report: simulator — space based radar, Vol. I: requirements, design and user guide*. Defence Research Establishment Ottawa (DREO), Contractor Report DND/SST File No. W7714-8-0141.

Raney, R.K. 1971. Synthetic aperture imaging radar and moving targets. *IEEE Transactions on Aerospace and Electronic Systems*, Vol. AES-7, No. 3, pp. 499–505.

Shapiro, I.I., Zisk, S.H., Rogers, E.E., Slade, M.A., and Thompson, T.W. 1972. Lunar topography: global determination by radar. *Science (Washington, D.C.)*, Vol. 178, pp. 939–948.

Sikaneta, I., Gierull, C.H., and Chouinard, J.-Y. 2003. Metrics for SAR-GMTI based on Eigen-decomposition of the sample covariance matrix. In *Radar 2003, Proceedings of the IEEE International Conference on Radar*, 3–5 Sept. 2003, Adelaide, Australia. IEEE, New York. [CD-ROM].

Skolnik, M. 1990. *Radar handbook*. 2nd ed. McGraw-Hill, New York.

Soumekh, M. 1997. Moving target detection in foliage using along-track monopulse synthetic aperture radar imaging. *IEEE Transactions on Image Processing*, Vol. 6, No. 8, pp. 1148–1163.

Stimson, G.W. 1998. *Introduction to airborne radar (aerospace and radar systems)*. 2nd ed. SciTech Publishing, Raleigh, N.C. Chapt. 24, p. 318.

Stockburger, E.F., and Held, D.N. 1995. Interferometric moving ground target imaging. In *Proceedings of the IEEE International Radar Conference*, 8–11 May 1995, Alexandria, Va. IEEE, New York. pp. 438–443.

Zisk, S.H. 1972. Lunar topography, first radar-interferometer measurements of the Alphonsus–Ptolenaeus–Arzachel region. *Science (Washington, D.C.)*, Vol. 178, pp. 977–980.